Earthquakes and Structures, *Vol. 17, No. 4 (2019) 399-409*
DOI: https://doi.org/10.12989/eas.2019.17.4.399

Pseudo-dynamic and cyclic loading tests on a steel-concrete vertical hybrid structure

Bo Wang[1a], Tao Wu[1b], Huijuan Dai[2c], Guoliang Bai[3d] and Jian Wu[*4]

[1]School of Civil Engineering, Chang'an University, Xi'an 710061, China
[2]School of Civil Engineering, Xi'an University of Science and Technology, Xi'an 710054, China
[3]School of Civil Engineering, Xi'an University of Architecture and Technology, Xi'an 710055, China
[4]Shaanxi Key Laboratory of Safety and Durability of Concrete Structures, Xijing University, Xi'an, 710123, China

(*Received April 21, 2019, Revised August 23, 2019, Accepted August 28, 2019*)

Abstract. This paper presents the experimental investigations on the seismic performance of a peculiar steel-concrete vertical hybrid structural system referred to as steel truss-RC tubular column hybrid structure. It is typically applied as the supporting structural system to house air-cooled condensers in thermal power plants (TPPs). Firstly, pseudo-dynamic tests (PDTs) are performed on a scaled substructure to investigate the seismic performance of this hybrid structure under different hazard levels. The deformation performance, deterioration behavior and energy dissipation characteristics are analyzed. Then, a cyclic loading test is conducted after the final loading case of PDTs to verify the ultimate seismic resistant capacity of this hybrid structure. Finally, the failure mechanism is discussed through mechanical analysis based on the test results. The research results indicate that the steel truss-RC tubular column hybrid structure is an anti-seismic structural system with single-fortification line. RC tubular columns are the main energy dissipated components. The truss-to-column connections are the structural weak parts. In general, it has good ductile performance to satisfy the seismic design requirements in high-intensity earthquake regions.

Keywords: steel-concrete hybrid structure; seismic performance; failure mechanism; pseudo-dynamic test; cyclic loading test

1. Introduction

Steel-concrete hybrid structures have been widely applied in practice, since they can make full use of different materials through scientific hybridization with different components made of reinforced concrete, steel and composite steel-concrete (Deierlein 2004, Ding 2016, Sivandi-Pour 2016, Dall'Asta 2017, Nguyen 2017, Dai 2018, Wang 2019). This paper focuses on a steel-concrete vertical hybrid structural system referred to as steel truss-RC tubular column hybrid structure. It is typically used for the supporting structure to house air-cooled condenser (ACC) system in thermal power plants (TPPs). As shown in Fig. 1, the lower parts are an array of RC thin-walled tubular columns with height of 30~40 m. The diameter is about 4 m, which is about 8~10 times of the thickness. Above the RC tubular columns, there is a steel truss space

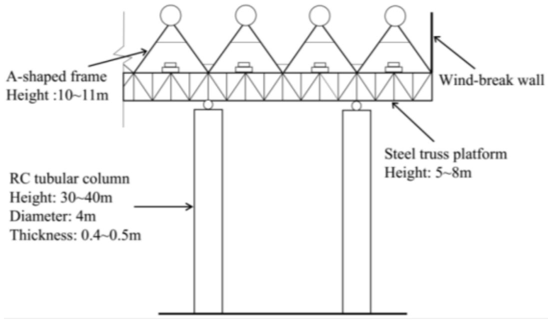

(a) Schematic diagram of supporting structure

(b) Supporting structure with exhaust steam pipes

Fig. 1 Supporting structure for air-cooled condenser (ACC) system

-platform about 5~8 m-height. On the steel truss platform, there are a series of A-shaped steel frames about 10~11 m-height. As a type of industrial building, a lot of huge-mass

*Corresponding author, Ph.D.
E-mail: wujian2085@126.com
[a]Associate Professor
E-mail: chnwangbo@chd.edu.cn
[b]Professor
E-mail: wutao@chd.edu.cn
[c]Lecturer
E-mail: daihuijuan1985@163.com
[d]Professor
E-mail: baiglgh@xauat.edu.cn

ISSN: 2092-7614 (Print), 2092-7622 (Online)

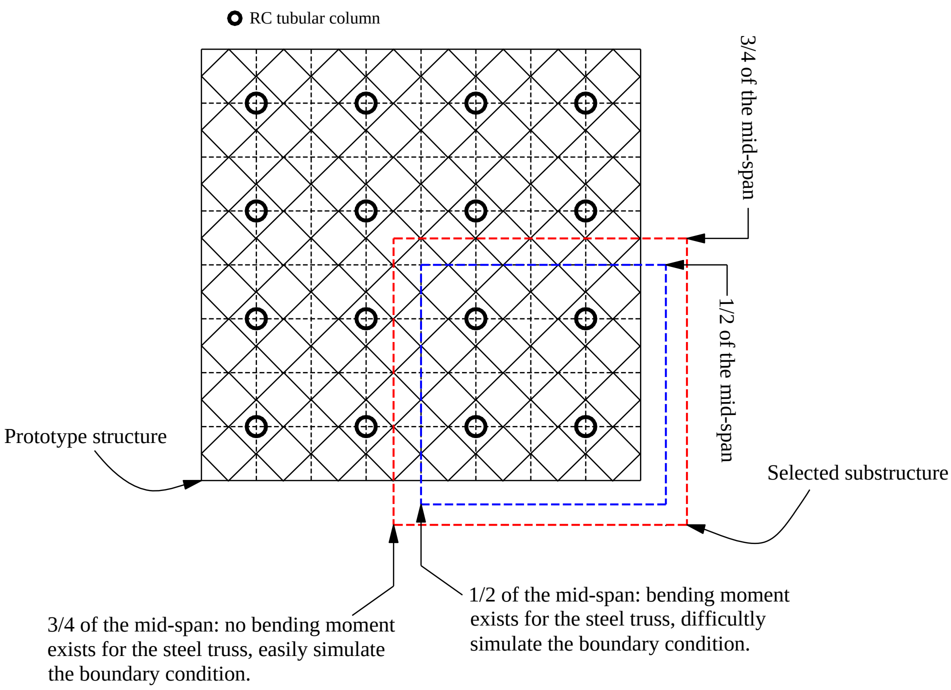

Fig. 2 Selection of the substructure from the prototype structure

Table 1 Main dimensions of components for the prototype structure and specimen

Component	Quantity	Value	
		Prototype structure	Specimen
RC tubular column	Number of columns	16	4
	Height	37.50 m	4687.5 mm
	External diameter	4 m	500 mm
	Wall thickness	0.4 m	50 mm
Steel truss platform	Height	7.5 m	937.5 mm
A-shaped steel frame	Height	10.36 m	129.5 mm

industrial units with 10,000 tons in weight (e.g., air-cooled condensers, exhaust steam pipes) are supported by the structure.

In the past, the supporting structure of ACC system was addressed rarely, while most of researches mainly focused on the ACC technology (Bredell 2006, Odabaee 2011, Borghei 2012, O' Donovan 2014, Berrichon 2015, Bustamante 2015). Since China is a country prone to earthquake disasters, it is necessary to investigate the seismic behavior of this kind of supporting structure. In this study, a range of pseudo-dynamic tests (PDTs) and a following cyclic loading test were conducted to investigate the seismic performance of this steel-concrete vertical hybrid structure.

2. Experimental program

2.1 Prototype building and scaled substructure

The prototype building is a 56 m-height air-cooled condenser supporting structure assumed to be located in high seismic region of China. According to the China seismic design code (GB 50011-2010, 2016), the seismic precautionary intensity is 8-degree with the peak ground acceleration (PGA) of 0.20 g. It means that when the earthquake with 10% probability of exceedance in 50 years occurs in this region, the seismic intensity is 8-degree and the corresponding PGA is 0.20 g. The site condition is class II. Due to the limitation of test field, a substructure about 1/4 of the prototype building was selected to conduct the specimen, as shown in Fig. 2. Since the bending moment exists in the mid-span of the steel truss, resulting in the difficult simulation of the boundary condition, 3/4 of the mid-span was taken to design the test specimen, in which no bending moment exists in the steel truss. For the length of the specimen, the scaling factor was determined as 1/8. Other scaling factors can be obtained through dimensional analysis (Kumar 1997). Table 1 summarizes the main dimensions of structural components for the prototype structure and specimen.

According to the China seismic design code (GB 50011-2010, 2016) and the seismic ground motion parameters zonation map of China (GB 18306-2015, 2015), the steel truss-RC tubular column hybrid structure should keep elastic under the frequent earthquake, should be in use after repairment under the basic earthquake, should not collapse under the rare and very rare earthquakes. The frequent, basic and rare earthquakes represent the earthquakes with 63.3, 10 and 2% probabilities of exceedances in 50 years, respectively. The very rare earthquake has 10-4 probability of exceedance in one year. The peak accelerations corresponding to the frequent, basic, rare and very rare earthquakes with the seismic precautionary intensity of 8-degree are 0.10, 0.20, 0.40 and 0.60 g, respectively.

2.2 Specimen and test setup

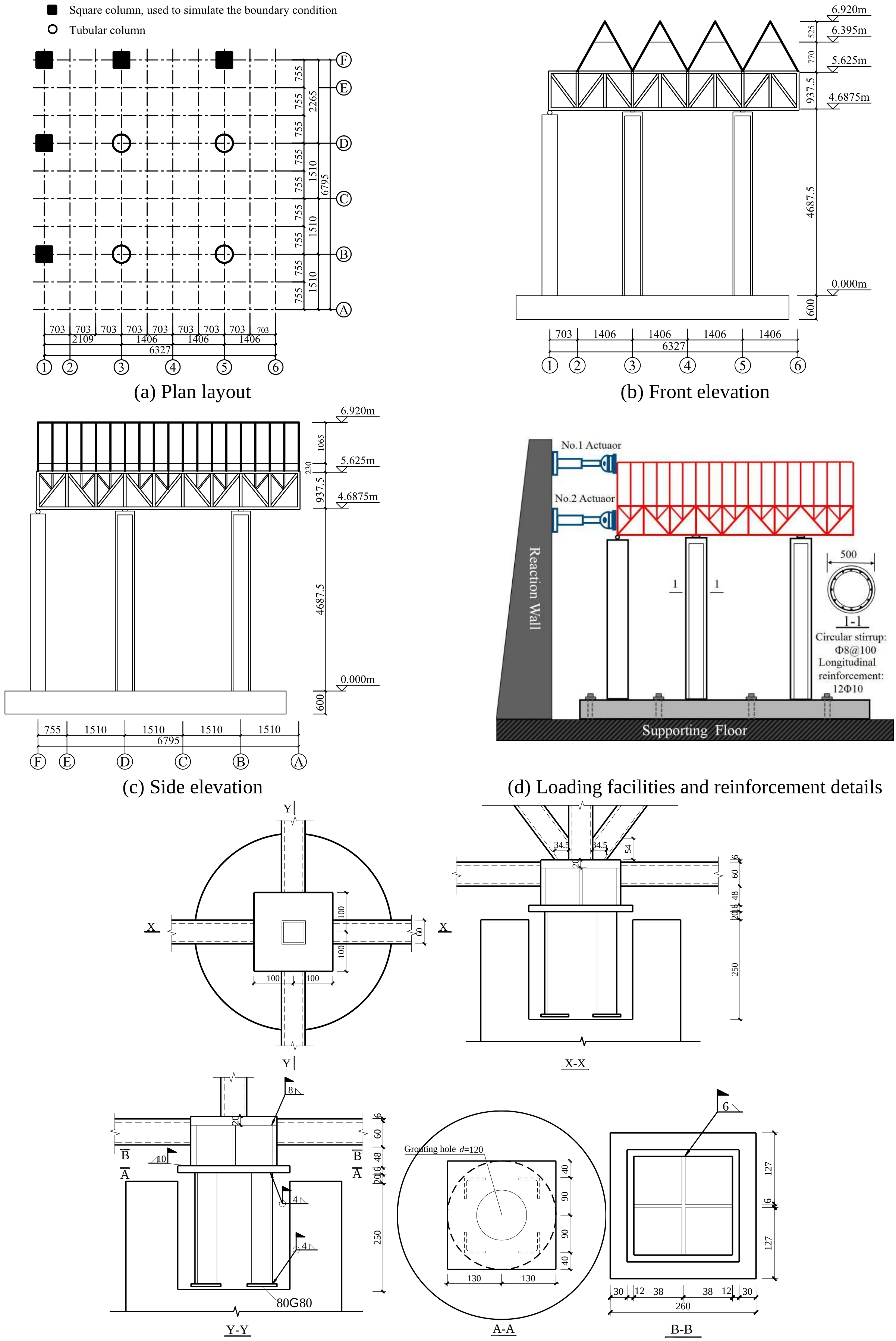

(e) Truss-to-column connection details

Fig. 3 Specimen and loading facilities (unit:mm)

Table 2 Material properties of the specimen

Component	Material	Strength grade	Position of Sampling	Cross section (mm)	F_y (MPa)	F_u (MPa)	ε_y (10^{-6})	E (MPa)
Steel truss	Steel tubes	Q235	Diagonal web member	60×2.5*	233	350	1165	2×10^5
				60×2.0**	242	366	1210	
			Vertical web member	60×2.5*	233	350	1165	
				50×1.5**	267	401	1335	
			Chord member	60×2.5	233	350	1165	
A-shaped frame			Horizontal beam / Diagonal column	25×1.5	240	363	1200	
Tubular column	Steel rebar	HRB400	Longitudinal rebar	10	475	713	2500	2×10^5
		HPB300	Stirrup	8	292	444	1460	1.9×10^5
	Concrete	C40		50	f_{cm} = 39.8 MPa			3.2×10^4

Note: *represents the web members located on the top of column; **represents the web members not on the top of column.

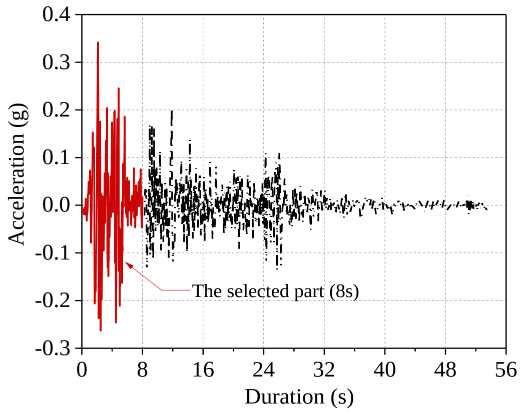

Fig. 4 The original input ground motion for PDTs

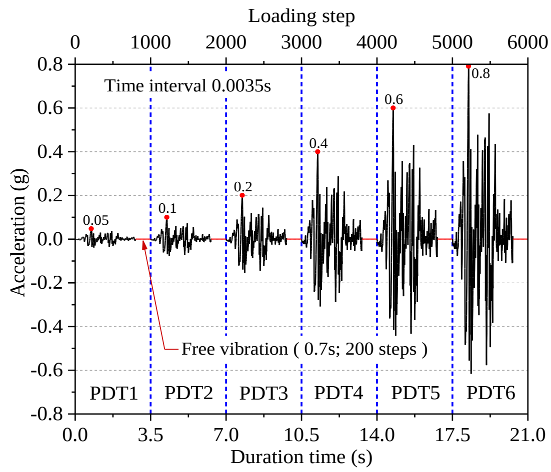

Fig. 5 Loading sequences of PDTs

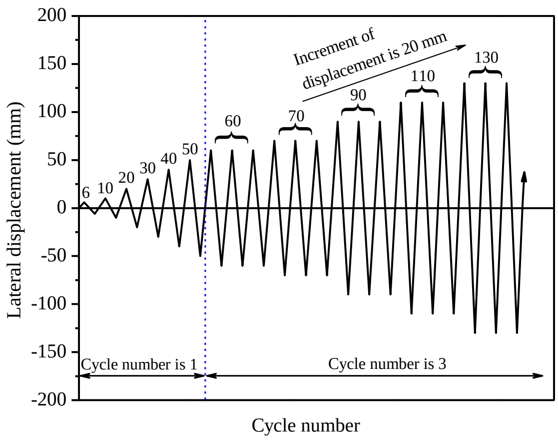

Fig. 6 Cyclic loading protocol

Fig. 3 shows the plan layout, elevations, loading facilities, reinforcement details and truss-to-column connection details of the specimen. Five square concrete columns were designed to simulate the boundary condition, as shown in Fig. 3(a). As shown in Fig. 3(d), two hydraulic actuators were respectively fixed to the reaction wall at the middle part of steel truss platform and the top of A-shaped frame. The truss is connected to the supporting columns by rigid connections, as shown in Fig. 3(e). Considering there were no proper shaped steel to simulate the scaled steel truss, square hollow steel tubes were selected to fabricate the steel truss in the specimen. Each tubular column was reinforced by twelve longitudinal steel rebars with diameter of 10 mm and 8 mm-diameter stirrups with space of 100 mm. The test material properties of the specimen are provided in Table 2. C40 grade concrete with the nominal compressive cube strength of 40 MPa was used for the tubular columns. The average compressive strength of concrete was obtained through compressive test of concrete cubes with 150 mm in side length. Q235 grade steel with the nominal yield strength of 235 MPa was used for the steel truss and A-shaped frames. The yield strength, ultimate strength, yield strain and elastic modulus of the materials under static loads are summarized in Table 2.

2.3 Loading program

In this study, the initial 8 s of El-Centro (NS) record was selected as the input ground motion to conduct PDTs, as shown in Fig. 4. The specimen was subjected to six hazard level with PGAs of 0.05, 0.10, 0.20, 0.40, 0.60 and 0.80 g, as shown in Fig. 5. Through dimensional analysis, the scaled duration and time interval of the input ground motion were determined as 2.8 s and 0.0035 s, respectively. A free vibration with duration of 0.7 s was added for each loading case to investigate the dynamic characteristics of the specimen. After the final loading case of PDTs, a cyclic loading test was conducted to investigate the ultimate

Table 3 Maximum base shear forces, lateral displacements and drift ratios of the specimen

PGA (g)	Maximum base shear force (kN)		Maximum lateral displacement (mm)				Maximum roof drift ratio (%)	
			Middle of truss		Top of A-shaped frame			
	+	−	+	−	+	−	+	−
0.05	10.29	11.48	0.88	1.56	1.39	2.61	0.02	0.04
0.10	16.35	14.35	2.35	1.98	3.22	3.17	0.05	0.05
0.20	27.93	29.32	4.87	4.46	6.56	6.67	0.09	0.10
0.40	46.73	47.97	11.26	12.30	14.38	15.77	0.21	0.23
0.60	61.94	65.42	21.40	21.63	23.79	25.76	0.34	0.37
0.80	102.15	82.80	45.73	33.67	55.83	37.27	0.81	0.54

seismic resistant capacity of the specimen. Fig. 6 shows the cyclic loading protocol. The amplitude of lateral displacements were controlled in cooperation with China specification for seismic test of building (JGJ 101/T-2015, 2015).

The base shear force method was utilized to calculate the restoring force provided by the actuators as follows (Mahin 1985, Nakashima 1992)

$$\hat{R}_i = \left(\frac{\sum F_i u_i}{\sum F_i} \right) \cdot V_B \tag{1}$$

where $\hat{R}_i$ is the restoring force obtained from the i-th hydraulic actuator, V_B is the base shear force, F_i is the exterior force applied at i-th floor, u_i is the modal displacement at i-th floor.

The mass matrix of specimen at each position of the loading actuator (as shown in Fig. 3(d)) was derived as follows

$$M = \begin{pmatrix} m_1 & \\ & m_2 \end{pmatrix} = \begin{pmatrix} 21830 & \\ & 9081 \end{pmatrix} kg \tag{2}$$

The first mode of natural vibration was used as the basic displacement mode as follows

$$\phi_1 = \{1 \quad 0.707\}^T \tag{3}$$

The loading ratio between the two actuators was derived by the first mode vibration and mass matrix as follows

$$F = \{F_1 : F_2\} = M \times \phi = \{2.34 : 1\} \tag{4}$$

3. Experimental results and discussion

3.1 Base shear force and lateral displacement

Table 3 summarizes the maximum base shear forces, lateral displacements and roof drift ratios of the specimen under PDTs. Fig. 7 shows the roof drift ratio time-histories of the specimen subjected to the incremental PGAs. It can be observed that the occurring moment of peak drift response was delayed with the increase of PGA due to the stiffness deterioration. Fig. 8 shows the the roof drift ratio versus base shear force hysteresis curves subjected to the

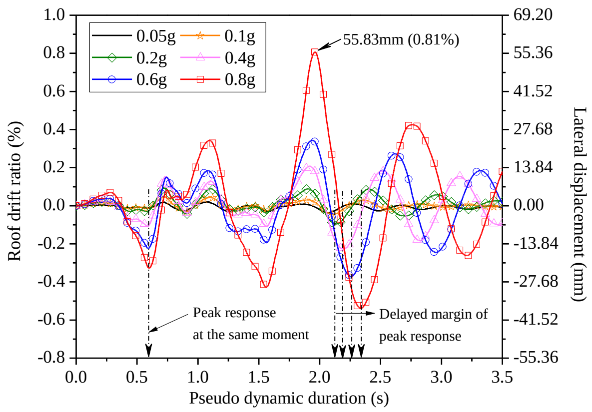

Fig. 7 Roof drift ratio time-histories of the specimen under PDTs

incremental PGAs. It can be seen that the initial and unloading stiffness of the specimen progressively decreased with the increase of PGA. In addition, the maximum roof drift ratio of the specimen increased sharply when the PGA increased from 0.60 g to 0.80 g, and the area of hysteresis loop with PGA of 0.80 g was much larger than that of 0.60 g. This indicated that the specimen damaged severely after the PGA came up to 0.80 g.

3.2 Deterioration behavior

Strength and stiffness deterioration has fatal influences on the seismic capacity of structural systems (Ibarra 2005). With the increase of PGA under PDTs, the strength and stiffness of specimen would deteriorate gradually. The secant stiffness K_i of the specimen was adopted to investigate the stiffness deterioration characteristics, which can be calculated by Eq. (5) (Wang 2017, Wang 2018)

$$K_i = \frac{|+F_i| + |-F_i|}{|+X_i| + |-X_i|} \tag{5}$$

where $+F_i$ and $+X_i$ are respectively the peak load and the corresponding lateral displacement under the i-th loading case of PDTs in the forward loading direction; $-F_i$ and $-X_i$ are respectively the peak load and the corresponding displacement under the i-th loading case of PDTs in the backward loading direction.

Furthermore, in order to evaluate the stiffness deterioration degree of the specimen with the increase of PGA, the relative stiffness ratio kre is defined by Eq. (6).

$$k_{\mathrm{re}} = \frac{K_i}{K_1} \times 100\% \tag{6}$$

where K_i is the secant stiffness of the specimen under each loading case of the PDTs calculated by Eq. (6); K_1 is the secant stiffness of the specimen under the first loading case when PGA equaled to 0.05 g. Specially, when PGA is 0.05 g, the relative stiffness ratio kre is 100%.

Table 4 summarizes the calculation results of dynamic characteristic parameters and lateral stiffness of the specimen under PDTs. Fig. 9(a) shows the stiffness and relative stiffness ratio of the specimen with increase of the

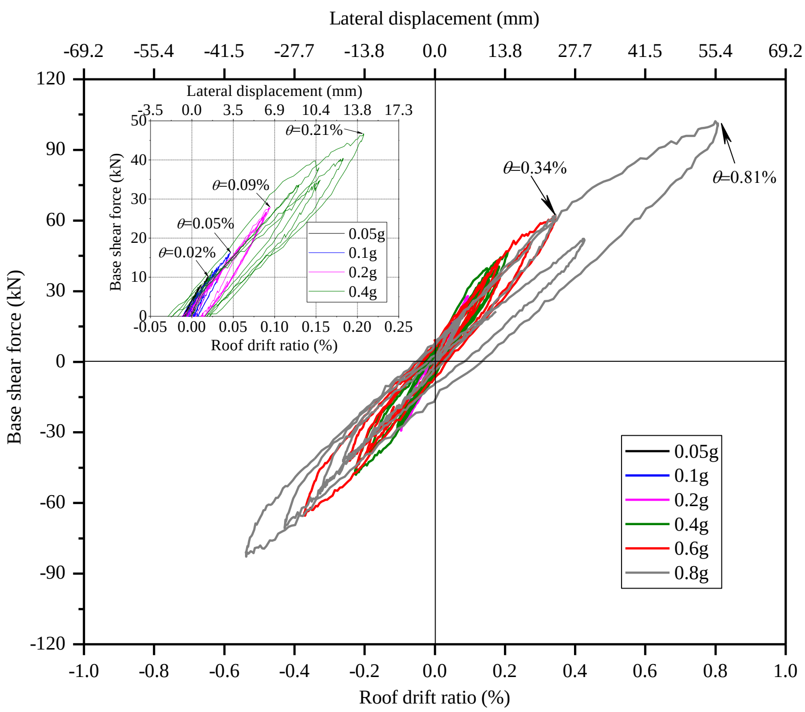

Fig. 8 Roof drift ratio versus base shear force hysteresis curves under PDTs

Table 4 Dynamic characteristic parameters and lateral stiffness of the specimen

PGA (g)	Fundamental Period (s)	Damping ratio (%)	Dynamic magnification factor	Lateral stiffness (kN/mm)	Relative stiffness ratio (%)
0.05	0.35	3.6	1.46	7.74	100
0.10	0.38	8.0	1.39	5.56	71.9
0.20	0.50	12.2	1.36	4.64	60.0
0.40	0.64	10.7	1.28	2.90	37.5
0.60	0.72	10.2	1.20	2.87	37.1
0.80	0.88	11.6	1.07	2.20	28.5

PGA. It can be seen that the stiffness deterioration process can be divided into two phases. Before the PGA came up to 0.40 g, the stiffness deteriorated sharply, then after that the stiffness deteriorated slowly. When the PGA equaled to 0.40 g, the stiffness decreased about 62.5% compared with that under the PGA of 0.05 g. This coincided with the experimental phenomenon that the noticeable cracks were firstly observed on the RC tubular columns when the PGA was equal to 0.40 g. Due to the stiffness deterioration of the specimen, the fundamental period would increase. Fig. 9(b) shows the fundamental period of the specimen with increase of the PGA. It was observed that the fundamental period almost increased linearly with increase of the PGA. Fig. 9(c) shows the damping ratio of the specimen with increase of the PGA. It can be seen that the damping ratio increased sharply before PGA came up to 0.20 g, however, it had no obvious changes when the PGA was greater than 0.20 g. When PGA came up to 0.80 g, the damping ratio was about 3.22 times of its initial value. Fig. 9(d) shows the dynamic magnification factor of the specimen with increase of the PGA. It can be observed that the magnification factor of the specimen decreased linearly with increase of the PGA.

Moreover, in order to investigate the deterioration behavior of the specimen more comprehensively, a coefficient k_{det} was defined by Eq. (7). It can be reflected by the slope of the maximum roof drift ratio or the base shear force versus PGA curves.

$$k_{\mathrm{det}} = \frac{\Delta(\mathrm{PGA})}{\Delta(\theta_{\mathrm{r}}, F_{\mathrm{b}})} \quad (7)$$

where Δ(PGA) is the increment of PGA, which is used to represent the intensity measure increment; $\Delta(\theta_r)$ and $\Delta(F_b)$ are respectively the increments of maximum roof drift ratio θ_r and maximum base shear force F_b, which are used to represent the response measure increment.

As shown in Figs. 9(e)-(f), two phases including linearity and softening were observed. When the PGA was greater than 0.60 g, the softening branch occurred.

3.3 Energy dissipation characteristics

The cumulated hysteresis dissipated energy of the specimen can be calculated by Eq. (8) (Wang 2018).

$$E_{\mathrm{h}} = \sum_{0}^{n} \frac{1}{2}(F_{i+1} + F_i)(X_{i+1} - X_i) \quad (8)$$

where F_{i+1} and X_{i+1} are respectively the restoring force and the corresponding lateral displacement at the i+1th time point; F_i and X_i are respectively the restoring force and the corresponding lateral displacement at the i-th time point.

Moreover, in order to investigate the energy dissipating degree of the specimen with increase of the PGA, the relative dissipated energy ratio was defined as the ratio of the cumulated hysteresis dissipated energy under each loading case of PDTs to that under the final loading case of PDTs with PGA of 0.8 g.

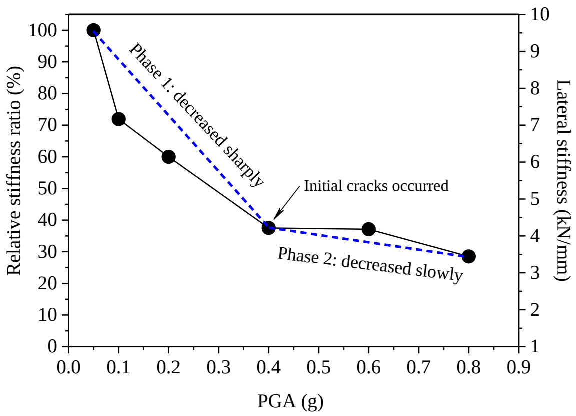

(a) Relative stiffness ratio and stiffness versus PGA

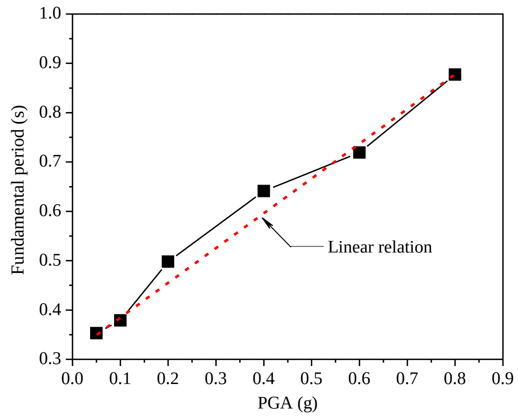

(b) Fundamental period versus PGA

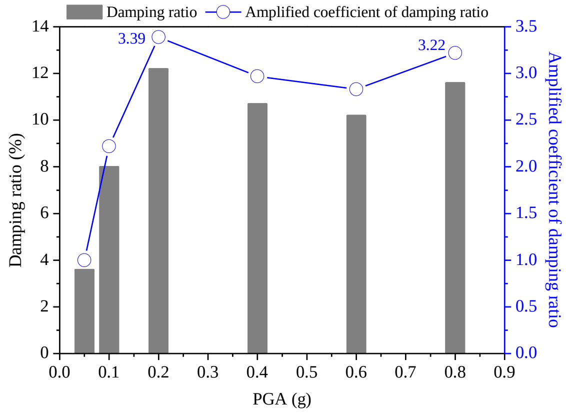

(c) Damping ratio versus PGA

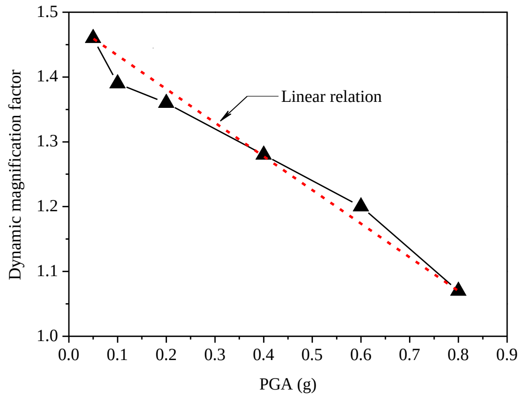

(d) Dynamic magnification factor versus PGA

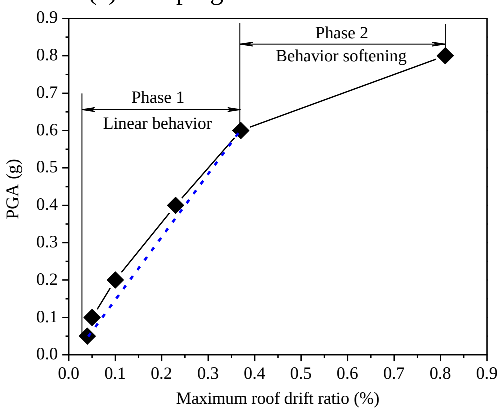

(e) Maximum roof drift ratio versus PGA

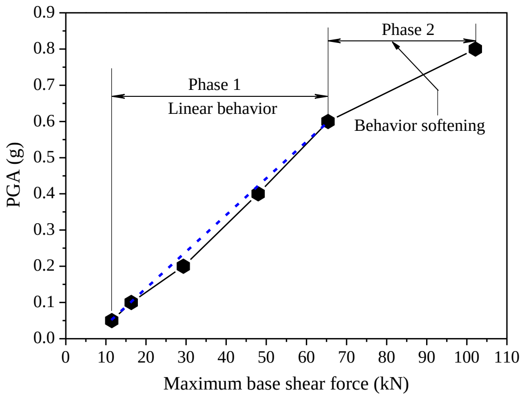

(f) Maximum base shear force versus PGA

Fig. 9 Deterioration behavior of the specimen under PDTs

Fig. 10(a) shows the time-history curves of cumulated hysteresis dissipated energy under PDTs. Fig. 10(b) shows the maximum cumulated hysteresis dissipated energy and the relative dissipated energy ratio of the specimen with increase of the PGA. It can be observed that the increase process of the cumulated hysteresis dissipated energy can be divided into three phases including the slow increase, quick increase and sharp increase. When the PGA came up to 0.20 g, the cumulated hysteresis dissipated energy increased quickly due to the stiffness deterioration and the plastic deformation. After the PGA reached 0.60 g, the cumulated hysteresis dissipated energy increased sharply.

In addition, the equivalent viscous damping coefficient of the specimen can be calculated by Eq. (9) (see Fig. 10(c)) (Wang 2017). It is widely used to evaluate the energy dissipation capacity of the specimen.

$$\xi_e = \frac{1}{2\pi} \frac{S_{ABC} + S_{CDA}}{S_{OBE} + S_{ODF}} \tag{9}$$

where S_{ABC} and S_{CDA} are the areas formed by curves ABC and CDA, respectively; S_{OBE} and S_{ODF} are the areas of right triangles OBE and ODF, respectively.

Fig. 10(d) presents the equivalent viscous damping coefficient versus PGA curve of the specimen. It can be seen that the equivalent viscous damping coefficient increased quickly before PGA came up to 0.2 g. When the PGA was greater than 0.2 g, the equivalent viscous damping coefficient increased slowly.

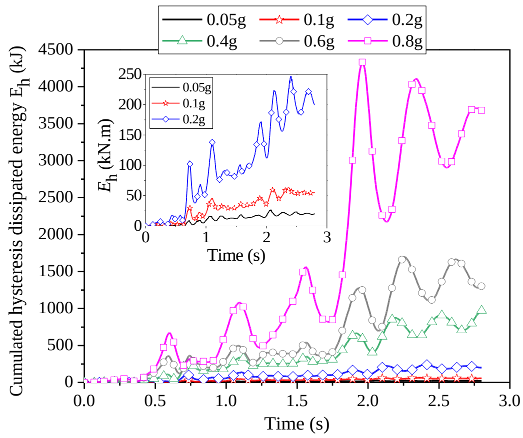

(a) Hysteresis dissipated energy time-history curves

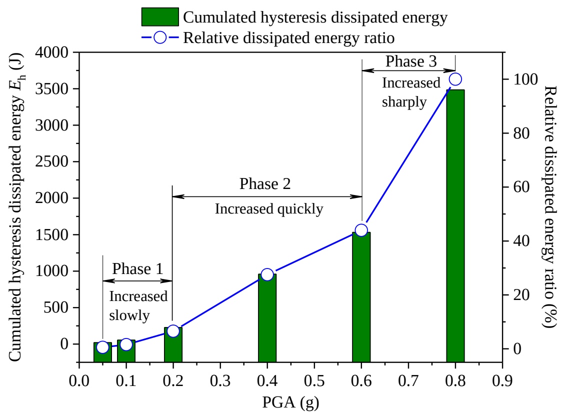

(b) Maximum cumulated hysteresis dissipated energy

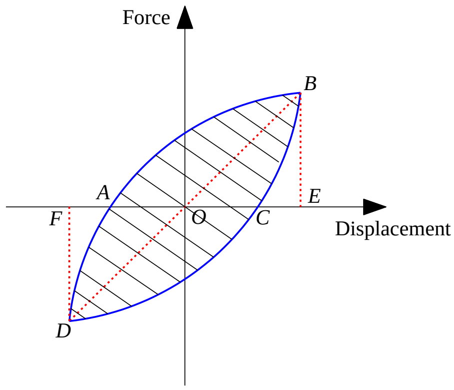

(c) Schematic diagram of calculation method for equiva lent damping coefficient

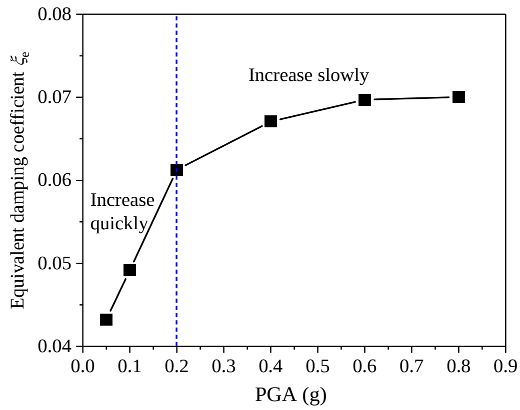

(d) Equivalent damping coefficient versus PGA

Fig. 10 Energy dissipation characteristics of the specimen

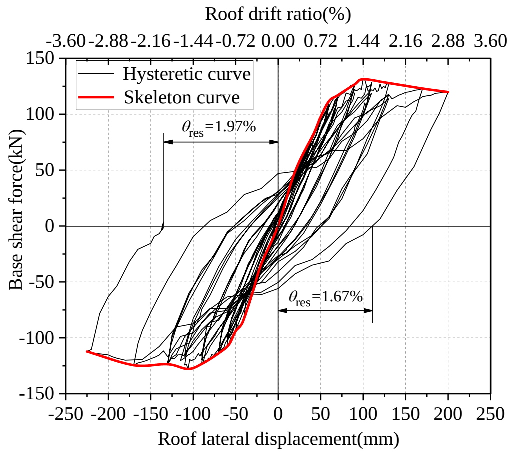

Fig. 11 Hysteretic behavior of the specimen

3.4 Ultimate seismic resistant behavior

Through the cyclic loading test after the final case of PDTs, the ultimate seismic resistant behavior of the specimen was investigated. Fig. 11 shows the hysteretic and skeleton curves for the base shear force versus roof lateral displacement (roof drift ratio). Table 5 lists the hysteretic characteristics of the specimen. The calculation results indicated that the ductility coefficient of the specimen was larger than 4, indicating that this kind of hybrid structure has good ductile performance. Fig. 12(a) shows the cumulated hysteresis dissipated energy versus lateral displacement curve. Fig. 12(b) shows the equivalent viscous damping coefficient versus lateral displacement curve. It can be observed that the cumulated hysteresis dissipated energy increased slowly before the control displacement came up to 60 mm, then after that it increased quickly due to the further propagation and extension of cracks. For the equivalent viscous damping coefficient, two phases were observed with the increase of control displacement. When the control displacement was small, since the cracks did not propagate and extend, nearly no more energy was dissipated, resulting in the decrease of equivalent viscous damping coefficient. However, with the increase of control displacement, the equivalent viscous damping coefficient increased quickly.

4. Failure mechanisms

With the increase of PGA under PDTs, the specimen sustained slowly accumulative damage. When the PGA equaled to 0.40 g, the noticeable crack was firstly observed on the bottom of RC tubular column. With increase of the PGA, cracks formed and developed on the column gradually. After the final loading case of PDTs with PGA of 0.80 g, cracks developed to the height of 2.2 m larger than

Table 5 Hysteretic characteristics of the specimen

Loading direction	Yield roof drift ratio (%)	Yield load (kN)	Peak load (kN)	Peak roof drift ratio (%)	Ultimate roof drift ratio (%)	Ductility coefficient
Forward (+)	0.72	97.42	131.17	1.45	2.89	4.01
Backward (-)	0.72	94.16	131.31	1.53	3.25	4.51

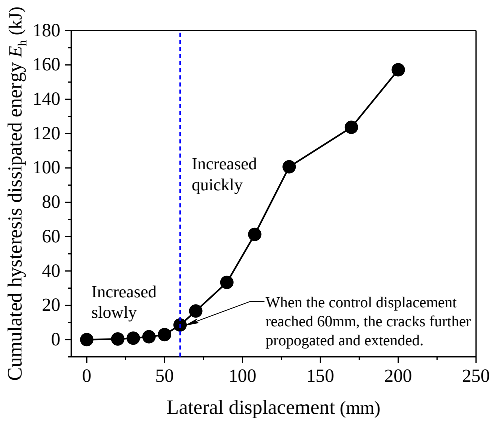

(a) Cumulated hysteresis dissipated energy versus lateral displacement

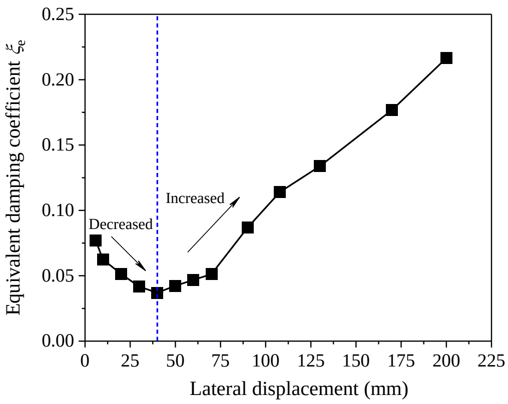

(b) Equivalent damping coefficient versus lateral displacement

Fig. 12 Energy dissipation characteristics of the specimen

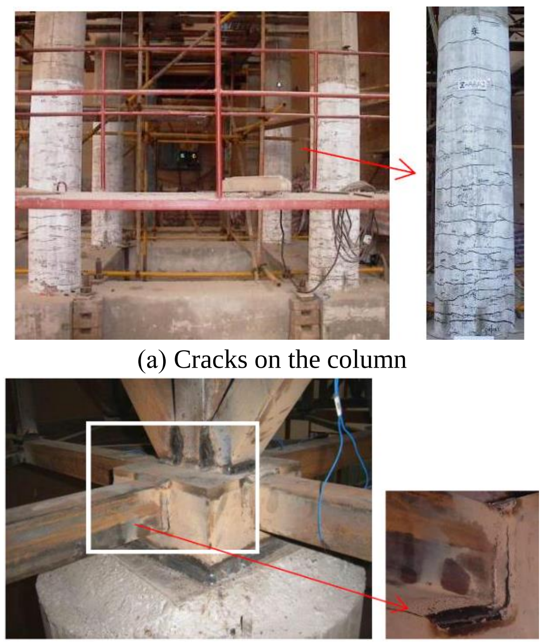

(a) Cracks on the column

(b) Fracture of elements in the steel truss

Fig. 13 Failure patterns of the specimen

1/3 of the full height of column, as shown in Fig. 13(a). Then, cracks on the columns further propagated and extended with increase of the control lateral displacement during the following cyclic loading test. In addition, it was observed that the elements in the steel truss on the top of column yielded and fractured, as shown in Fig. 13(b).

In order to reveal the failure mechanism of the specimen, mechanical analysis were conducted. Fig. 14(a) shows the mechanical model of the specimen, where F_1 and F_2 were lateral actions in accordance with the experimental loading program. Under the lateral forces, the actions were transferred from A-shaped steel frames to steel truss in the terms of bending moment, shear force and axial force of the elements. As shown in Fig. 14(a), the bending moment along the height of column mainly distributed at the bottom. This can be accounted for the failure phenomenon why the cracks mainly occurred at the bottom of columns. Fig. 14(b) shows the structural inner action analysis on the top part of column. It can be found that all the forces were transferred from the superstructure to the substructure through the truss-to-column connection. Moreover, the lower chord of the steel truss borne the bending moment. This can be accounted for the failure phenomenon why the elements in the steel truss on the top of column fractured.

Based on the discussion previously, it can be concluded that the steel truss-RC tubular column hybrid structure is an anti-seismic structural system with single-fortification line and RC tubular columns are the main energy dissipated components. It is similar to a bridge with RC columns and a deck (Chisari 2015). In order to improve the energy dissipation capacity of columns, stirrup densification were recommended. Besides, the truss-to-column connections were the weak parts for this hybrid structure which should be designed stronger enough. It is noted that this study just presents the experimental research results of the specimen which is a scaled substructure of the prototype building. So as to investigate the seismic behavior of this kind of steel-concrete hybrid structural system more comprehensively, the numerical simulations on the prototype structure will be conducted to make deep analysis in the subsequent study.

5. Conclusions

This paper investigated the seismic performance of a steel-concrete vertical hybrid structure referred to as steel truss-RC tubular column hybrid structure through PDTs and a following cyclic loading test. The main conclusions can be drawn as follows:

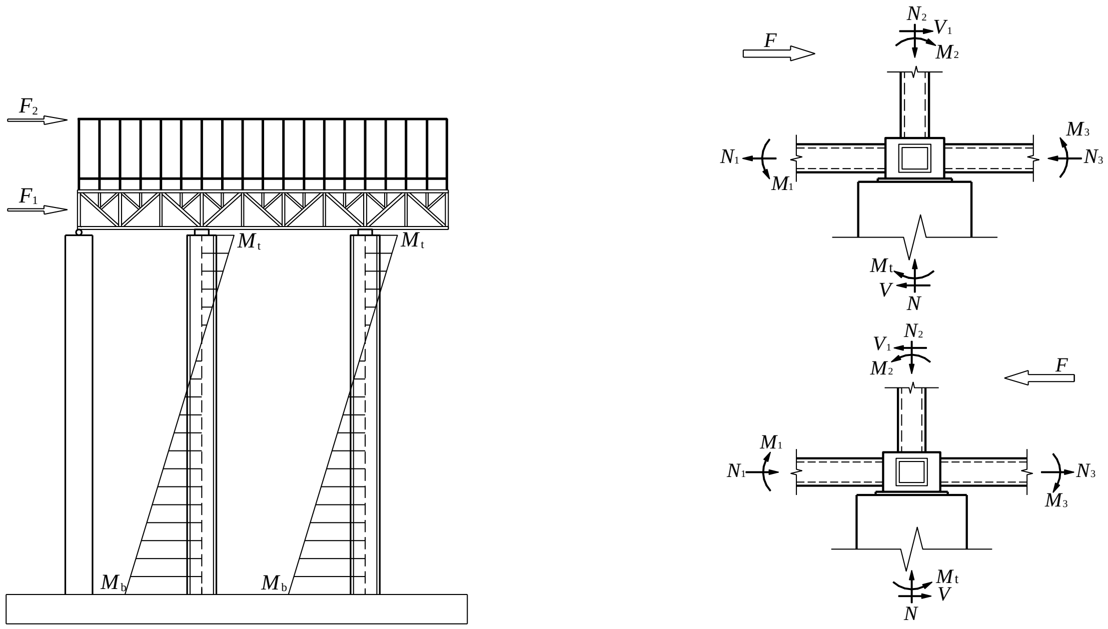

(a) Distribution pattern of bending moment along the column (b) Structural inner action analysis on the top part of column

Fig. 14 Mechanical analysis of the specimen

• The steel truss-RC tubular column hybrid structure is an anti-seismic structural system with single-fortification line. RC tubular columns are the main energy dissipated components for this kind of structure. In order to improve the energy dissipation capacity of columns, stirrup densification were recommended. In addition, the truss-to-column connections are the structural weak parts which should be designed stronger enough.
• The results of PDTs showed that the steel truss-RC tubular column hybrid structure had the obvious deterioration characteristics with increase of the PGA. After the final loading case of PDTs, the lateral stiffness decreased to 28.5% of its initial value. Along with the deterioration of lateral stiffness, the fundamental period almost increased linearly with increase of the PGA. The damping ratio increased sharply before PGA came up to 0.20 g, however, when the PGA was greater than 0.20 g, it had no obvious changes with increase of the PGA. The magnification factor of the specimen decreased linearly with increase of the PGA. Two phases including linearity and softening were observed in the maximum roof drift ratio versus PGA curve and the base shear force versus PGA curve. The softening branch occurred when PGA was greater than 0.60 g.
• Analysis of energy dissipation characteristics of the specimen indicated that the increase process of the cumulated hysteresis dissipated energy with increase of the PGA could be divided into three phases including the slow increase, quick increase and sharp increase. It increased quickly after PGA came up to 0.20 g due to the stiffness deterioration and plastic deformation. For the equivalent viscous damping coefficient, it increased quickly before PGA came up to 0.20 g. However, it increased slowly when the PGA was greater than 0.20 g.
• The cyclic loading test results indicated that the ductility coefficient of the specimen was larger than 4, indicating that the steel truss-RC tubular column hybrid structure has good ductile performance. In general, it could satisfy the seismic design requirements in high-intensity earthquake regions.

Acknowledgments

Special thanks to Prof. Lihua Zhu from Xi'an University of Architecture Technology and chief engineer Dr. Hongxing Li from Northwest Electronic Power Design Institute for their helpful and valuable discussions on the experimental analysis. The work presented in this paper has been funded mainly by the National Natural Science Foundation of China (NSFC, Grant No. 51708037 and 51978076), Natural Science Foundation of Shaanxi Province (Grant No. 2019JQ-193), China Postdoctoral Science Foundation (Grant No. 2017M610616) and Xi'an Municipal Science and Technology Planning Project (Grant No. 201805045YD23CG29(6)).

References

Berrichon, J.D., Louahlia-Gualous, H., Bandelier, P., Clement, P. and Bariteau, N. (2015), "Experimental study of flooding phenomenon in a power plant refuex air-cooled condenser", *Appl. Therm. Eng.*, **79**, 214-224. https://doi.org/10.1016/j.applthermaleng.2014.11.070.

Borghei, L. and Khoshkho, R.H. (2012), "Computational fluid dynamics simulation on a thermal power plant with air-cooled condenser", *J. Power Energy*, **226**, 837-884. https://doi.org/10.1177/0957650912454821.

Bredell, J.R., Kroger, D.G. and Thiart, G.D. (2006), "Numerical investigation of fan performance in a forced draft air-cooled steam condenser", *Appl. Therm. Eng.*, **26**, 846-852. https://doi.org/10.1016/j.applthermaleng.2005.09.020.

Bustamante, J.G., Rattner, A.S. and Garimella, S. (2015), "Achieving near-water-cooled power plant performance with air-cooled condensers", *Appl. Therm. Eng.*, **72**, 1-10. https://doi.org/10.1016/j.applthermaleng.2015.05.065.

Chisari, C., Bedon, C. and Amadio, C. (2015), "Dynamic and static identification of base-isolated bridges using Genetic Algorithms", *Eng. Struct.*, **102**, 80-92. https://doi.org/10.1016/j.engstruct.2015.07.043.

Dai, H.J. and Wang, B. (2018), "Seismic analysis of steel solid web girder-RC tubular column hybrid structure", *Appl. Sci.*, **8**, 2095. https://doi.org/10.3390/app8112095.

Dall'Asta, A., Leoni, G., Morelli, F., Salvatore, W. and Zona, A. (2017), "An innovative seismic-resistant steel frame with reinforced concrete infill walls", *Eng. Struct.*, **141**, 144-158. https://doi.org/10.1016/j.engstruct.2017.03.019.

Deierlein, G.G. and Noguchi, H. (2004), "Overview of US-Japan research on the seismic design of composite reinforced concrete and steel moment frame structures", *J. Struct. Eng.*, **130**, 361-367. https://doi.org/10.1061/(ASCE)0733-9445(2004)130:2(361).

Ding, Y., Wu, M., Xu, L.H., Zhu, H.T. and Li, Z.X. (2016), "Seismic damage evolution of steel-concrete hybrid space-frame structures", *Eng. Struct.*, **119**, 1-12. https://doi.org/10.1016/j.engstruct.2016.04.007.

GB 18306-2015 (2015), Seismic Ground Motion Parameters Zonation Map of China, General Administration of Quality Supervision, Inspection and Quarantine of the People's Republic of China, Standardization Administration of the People's Republic of China, Beijing, China. (In Chinese)

GB 50011-2010 (2016), Code for Seismic Design of Buildings, Ministry of Housing and Urban-Rural Development of the People's Republic of China, General Administration of Quality Supervision, Inspection and Quarantine of the People's Republic of China; Beijing, China. (In Chinese)

Ibarra, L.F., Medina, R.A. and Krawinkler, H. (2005), "Hysteretic models that incorporate strength and stiffness deterioration", *Earthq. Eng. Struct. Dyn.*, **34**, 1489-1511. https://doi.org/10.1002/eqe.495.

JGJ 101/T-2015 (2015), Specification for Seismic Test of Buildings, Ministry of Housing and Urban-Rural Development of the People's Republic of China; Beijing, China. (In Chinese)

Kumar, S., Itoh, Y., Saizuka, K. and Usami, T. (1997), "Pseudo dynamic testing of scaled nodels", *J. Struct. Eng.*, **123**(4), 524-526. https://doi.org/10.1061/(ASCE)0733-9445(1997)123:4(524).

Mahin, S. and Shing, P.B. (1985), "Pseudo dynamic method for seismic testing", *J. Struct. Eng.*, **111**(7), 1482-1503. https://doi.org/10.1061/(ASCE)0733-9445(1985)111:7(1482).

Nakashima, M., Kato, H. and Takaoka, E. (1992), "Development of real-time pseudo dynamic testing", *Earthq. Eng. Struct. Dyn.*, **21**, 79-92. https://doi.org/doi:10.1002/eqe.4290210106.

Nguyen, Q.H., Tran, V.T. and Hjiaj, M. (2017), "Hybrid RC-steel members under bending and shear: Experimental investigation and design model", *J. Constr. Steel Res.*, **138**, 837-850. https://doi.org/10.1016/j.jcsr.2017.06.017.

O' Donovan, A. and Grimes, R. (2014), "A theoretical and experimental investigation into the thermodynamic performance of a 50 MW power plant with a novel modular air-cooled condenser", *Appl. Therm. Eng.*, **71**, 119-129. https://doi.org/10.1016/j.applthermaleng.2014.06.045.

Odabaee, M. and Hooman, K. (2011), "Application of metal foams in air-cooled condensers for geothermal power plants: An optimization study", *Int. Commun. Heat Mass Transfer*, **38**, 838-843. https://doi.org/10.1016/j.icheatmasstransfer.2011.03.028.

Sivandi-Pour, A., Gerami, M. and Kheyroddin, A. (2016), "Uniform damping ratio for non-classically damped hybrid steel concrete structures", *Int. J. Civil Eng.*, **14**, 1-11. https://doi.org/10.1007/s40999-016-0003-8.

Wang, B., Dai, H.J., Bai, Y.T. and Xiao, K. (2019), "Influence mechanism of steel diagonal braces on mechanical behavior of steel truss-RC tubular column hybrid structure", *J. Earthq. Eng*., 1-17. https://doi.org/10.1080/13632469.2019.1605317.

Wang, B., Dai, H.J., Wu, T., Bai, G.L. and Bai, Y.T. (2018), "Experimental investigation on seismic behavior of steel truss-RC column hybrid structure with steel diagonal braces", *Appl. Sci.*, **8**, 131. https://doi.org/10.3390/app8010131.

Wang, J.F. and Zhang, H.J. (2017), "Seismic performance assessment of blind bolted steel-concrete composite joints based on pseudo-dynamic testing", *Eng. Struct.*, **131**, 192-206. https://doi.org/10.1016/j.engstruct.2016.11.011.

CC